# Influence of Fissure Inclination on Deformation and Strain Distribution of **Damaged Materials Based on Digital Image Correlation Method**

# Hongwei WANG\*, Fuxiang XIE, Jian SONG, Xi FU, Zhaoming YIN

School of Machinery and Automation, Weifang University, Weifang 261061, China http://doi.org/10.5755/j02.ms.39856

Received 18 December 2024; accepted 6 February 2025

Sandstone-like specimens with fissures (fissure inclination 0°, 30°, 45°, 60°, 75°, 90°) were made for investigation into the influence of fissure inclination on deformation of damaged rock mass. The high-speed camera was used to record the deformation images of the specimen. Based on the digital image correlation (DIC) method, the strain distribution was calculated. The strain evolution pattern of fissured rock mass under the effect of fissures was analyzed via the maximum equivalent strain, average equivalent strain, and strain distribution, respectively. The results revealed that prefabricated fissure specimens exhibit four distinct phases: stable deformation, accelerated deformation, crack propagation and specimen failure. The DIC analysis revealed that the new cracks on the fissured specimens predominantly originate from the fissures' tips and propagate in a direction aligned with the principal stress. The maximum equivalent strain of the specimen was related to the fissure inclination. The maximum equivalent strain of the specimen with a fissure inclination of 90° and the intact specimen increased linearly. For fissure inclination between 0° and 75°, the strain of the specimen exhibited a pronounced increase following the accelerated deformation stage. The average equivalent strain of the specimen initially rose and then declined with the increase of the fissure inclination. The maximum value of the average equivalent strain was observed when the fissure was inclined approximately up to 45°.

Keywords: fissured specimen, digital image correlation, equivalent strain, sandstone-like materials.

#### 1. INTRODUCTION

The geological conditions, disturbance caused by excavation, and the blasting load exert an influence on the deep surrounding rock, which may result in zonal rupture phenomena. This leads to the formation of fissures, joints, and other damage on the structural surfaces. Furthermore, the geological movements result in considerable damage to the rock mass, reducing its structural integrity and stability. The impact of initial damage on the rock mass results in alterations to its mechanical properties and an increase in deformation. A comprehensive understanding of the mechanical properties and deformation mechanisms of damaged rock masses is of paramount importance for the safe and effective execution of deep engineering excavations, maintenance, and stability Consequently, scholars have conducted extensive research on the mechanical properties and deformation mechanisms of damaged rock masses.

In the 1990s, research was conducted on the process of damage extension in rocks with co. mputed tomography scanning [1, 2]. Zhang [3] examined the influence of mineral inclusions and pore structure on the deterioration of coals. It was found that the porosity and pore distribution within coals influence their strength. Wang<sup>[4]</sup> employed acoustic emission, potential and digital image correlation methods to monitor the damage process of heat-treated granite. The effects of heat treatment on the acoustic emission, potential and digital image correlation strain field patterns were investigated.

Furthermore, scholars were engaged in research examining the influence of internal damage on rock mechanical properties. This research was conducted from two distinct perspectives: the experimental and the theoretical.

Zhao [5] investigated the impact of pre-existing defects, including shape, size, number, and angle, on the mechanical properties and damage patterns of rocks. Li et al. [6] investigated the expansion and merging of pre-existing fissures in marble samples under compression. Which indicated that both winged (tensile) cracks and secondary (shear) cracks expand in a steady manner from the fissure tip. Wang [7] conducted uniaxial compression tests on rocklike specimens with curved ice-filled defects (Type I) and found that low temperature, defect morphology, and the presence of ice-filled defects had a significant effect on the mechanical properties. Li [8] conducted uniaxial cyclic loading tests on sandstone specimens with fissures of different angles. The evolution of energy indexes with peak load and crack angle was explored. Liu [9] conducted uniaxial compression experiments on granite specimens with a single prefabricated crack and investigated the effect of crack inclination on the crack initiation mechanism from the perspective of theoretical analysis. Tian [10] conducted freeze-thaw injury experiments on prefabricated fissured rock masses in submerged slip areas. Tang [11] conducted uniaxial compression tests on intact, single-fissure and cross-fissure specimens, respectively, to investigate the mechanical property and damage mechanisms of jointed rock masses under uniaxial compression test conditions. Song [12] conducted post-freeze-thaw uniaxial compression

\* Corresponding author: H. Wang

E-mail: 20200016@wfu.edu.cn

tests on saturated fissured red sandstone to investigate the effects of varying freeze-thaw cycles and fissure inclinations on the macroscopic mechanical properties. Quan [13] investigated the influence of freeze-thaw damage on the longitudinal wave velocity of sandstone specimens. Luo et al. [14] noted that the presence of fissure clusters resulted in a notable reduction in the compressive capacity of the specimens.

Cao et al. [15] investigated the stresses and deformations in deeply buried circular tunnels in rock masses, considering the effects of rock gravity and damage zones. Li et al. [16] established a multifactorial coupled damage ontology model under joint – loading considering the non-uniformity, anisotropy and initial structure of the rock volume, and illustrated the relationship between the damage evolution and the joint angle in the rock mass.

Zhao [17] analyzed the deformation of damaged rocks with digital image correlation method. Li [18] conducted experiments employing acoustic emission and digital image correlation to monitor changes in the mechanical and structural properties of defective granite specimens subjected to high-temperature cycling. Zhou [19] investigated the effect of defect geometry parameters and fissure angle on the cracking process with digital image correlation analysis. Zhu [20] investigated the evolutionary process of rock crack initiation and extension with 3D digital image correlation method. Wang [21] analyzed the precursors of full-field strain information using statistical methods based on digital image correlation. Maruschak [22] analyzed the effect of multi-cracking on the deformation behavior of 25Kh1MF steel and defined four different phases experienced by the pattern before damage.

However, previous studies on the deformation of damaged rock masses conducted by scholars have mostly analyzed the pattern of nominal strains calculated from deformations measured by displacement extensometers. The nominal strain can facilitate the evaluation of deformation behavior in rock masses subjected to damage, yet it does not offer a comprehensive representation of the surface strain distribution patterns observed in such rock masses. Consequently, the deformation images of the specimen surface are recorded with high-speed cameras, and the strain distribution on the surface of the damaged specimen is calculated based on the digital image correlation method. Furthermore, the strain parameter evolution pattern of the damaged rock mass is analyzed.

#### 2. MATERIAL AND EQUIPMENT

#### 2.1. Experimental material

In this paper, the sandstone in Zigong, Sichuan Province was used as a template, and sandstone-like materials with similar mechanical properties, deformation patterns, and damage pattern were prepared as experimental materials.

These materials were prefabricated fissures with different inclination angles in the middle of the specimen (see Fig. 1. for the specimen schematic), which allowed to simulate the damage. The prefabricated fissure specimens prepared have fissure inclination angles of  $\alpha$  in the middle of the specimen of  $0^{\circ}$ ,  $30^{\circ}$ ,  $45^{\circ}$ ,  $60^{\circ}$ ,  $75^{\circ}$ , and  $90^{\circ}$ . Six types of damages specimens were prepared, and intact specimens were prepared as a reference group for mechanical tests.

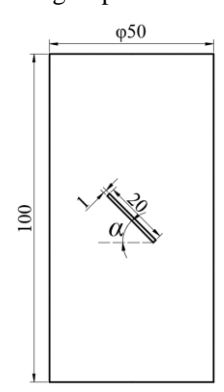


Fig. 1. Schematic diagram of the specimen with the prefabricated fracture

The aggregate of sandstone-like materials was 40 mesh river sand, cement was used for adhesive, and gypsum powder was used as a regulator. River sand: cement: gypsum powder: water = 2:1:0.05:0.7. The preparation method was referred to in literature [23], and some of the prepared are specimens were shown in Fig. 2. The main mechanical property parameters of sandstone and sandstone-like specimens are shown in Table 1.



Fig. 2. Part of prepared specimens

#### 2.2. Experimental equipment

The strain analysis system comprises a multifunctional material mechanics testing machine, a high-speed camera, a data acquisition card, and a computer (as shown in Fig. 3. The uniaxial compression test of Sandstone-like materials is conducted on the multifunctional material mechanics testing machine. The maximum load of the testing machine is 300 kN, with an accuracy of  $\pm$  50 N. Control of the loading speed is achieved through two methods: the displacement method and the load method.

Table 1. Principal mechanical property parameters of sandstone and sandstone-like specimens

Type	Density, g/cm <sup>3</sup>	Poisson's ratio	Strength, MPa	Elastic modules, GPa	
Sandstone	2.2 ~ 3.0	0.05 ~ 0.20	47 ~ 180	2.78 ~ 5.4	
Sandstone-like specimen	1.96 ~ 2.85	0.13 ~ 0.19	38 ~ 70	2.31 ~ 4.28	

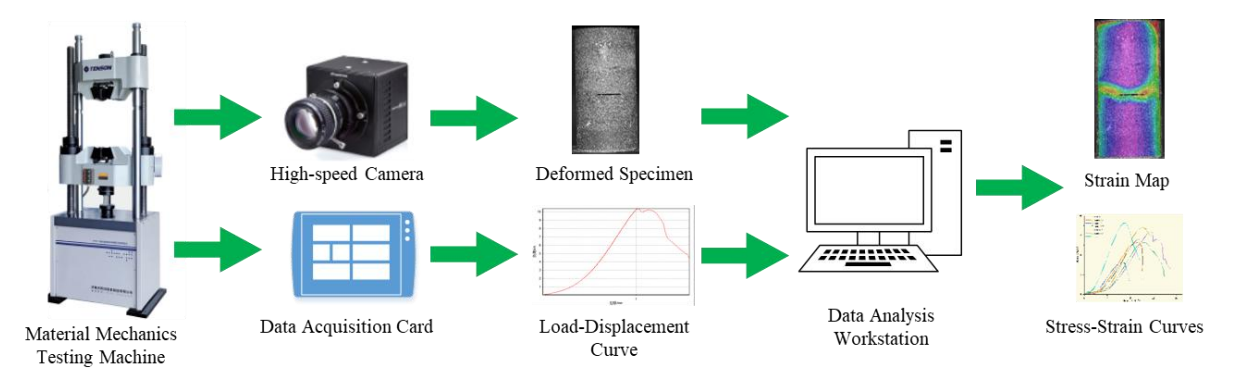


Fig. 3. Experimental flow chart

During the test, a high-speed camera is employed to document the deformation of the specimen surface. The camera utilized is Photron's FASTCAM Mini WX50, which has a maximum effective square resolution of 2048 × 2048 pixels.

## 3. EXPERIMENTAL PROCESS AND RESULTS

#### 3.1. Experimental design and process

In order to obtain the deformation image of the specimen, we employed the strain analysis system (as shown in Fig. 4) to conduct the mechanical test and deformation image acquisition Initially, compression tests were conducted on intact specimens and prefabricated fissures specimens(with fissure inclination of 0°, 30°, 45°, 60°, 75°, and 90°, respectively) with multifunctional material mechanics testing machine. To avoid the potential for significant discrepancies in test due to the discrete nature of the variables, three distinct mechanical tests were conducted for each type of specimens. The test was conducted with displacementcontrolled loading of the specimen, with the loading speed set at 1mm/min. When the specimen exhibited clear signs of cracking at the surface and lost its load-bearing capacity, the loading was terminated.

The High-speed camera Fastcam Mini WX50 was employed to document the deformation of the specimen surface. The shooting speed and shutter speed of the camera were 50 frames per second (fps) and 1/1000, respectively. Additionally, an LED flash was utilised to supplement the lighting, thereby facilitating the acquisition of a clear image of the specimen.

To analyze the distribution of the strain on the surface of the specimen and the strain evolution, the DIC method was employed to compare and calculate the deformed photographs with the reference photographs. This involved using the un-deformed specimen taken before the test as a reference. To reduce calculation error, the upper and lower contact surfaces of the specimen and the pressure sensor, as well as the positions of the left and right edges of the specimen, were ignored. Based on the results of numerous experiments and calculations, we recommended that the edge of the specimen be selected for the calculation of strain, with a distance of  $2 \sim 3$  mm inward from the initial point. This approach has been shown to minimize calculation error.

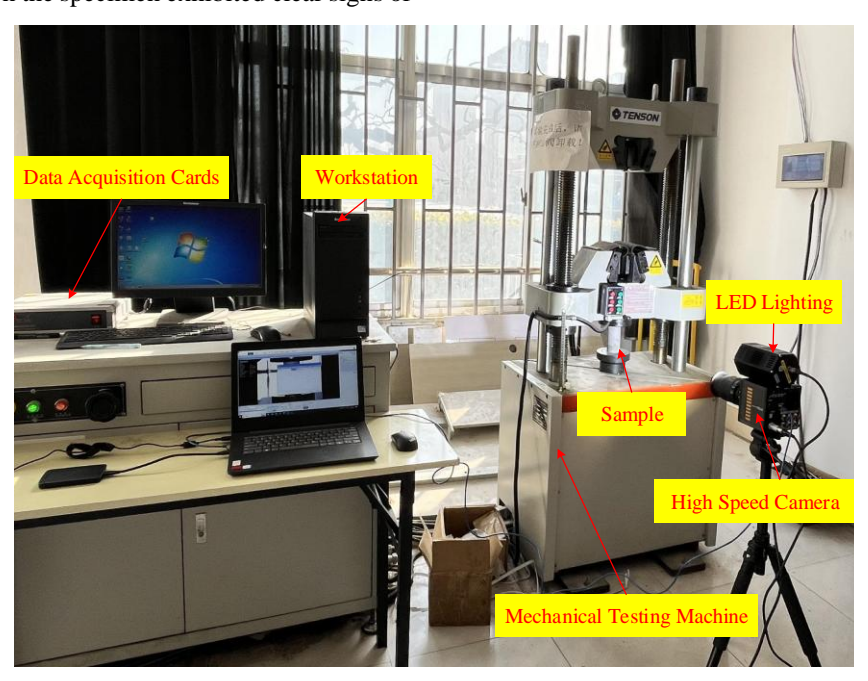
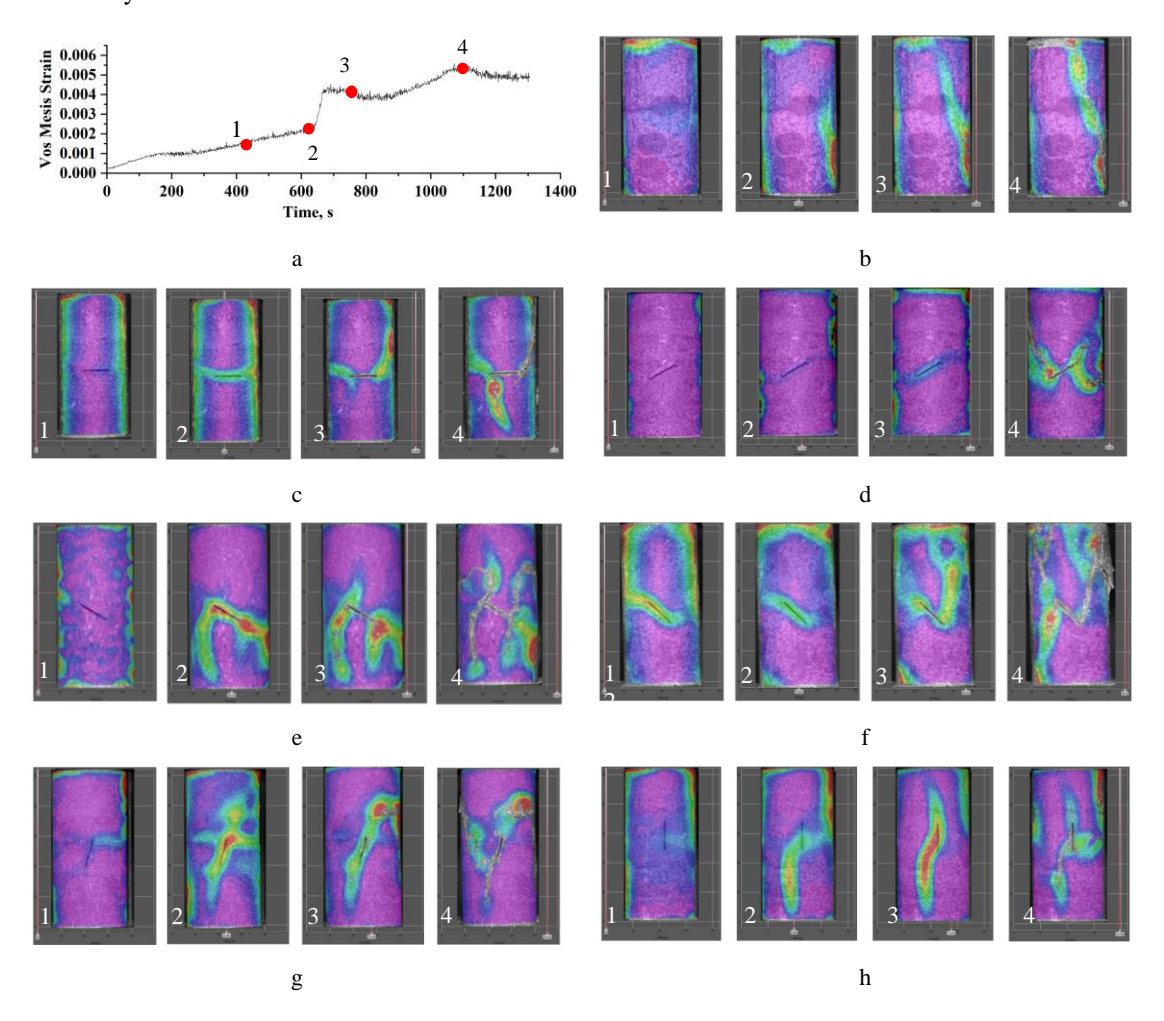


Fig. 4. Mechanical experiment system

#### 3.2. Experimental results

Uniaxial compression tests were conducted on intact and fissured specimens, the mechanical parameters and deformation images were obtained based on the material mechanics testing machine and high-speed camera, respectively. It was observed during the test that fissured specimens went through four stages: stable deformation stage (a), accelerated deformation stage (b), crack propagation stage (c), and specimen failure stage (d) (shown in Fig. 5 a). As for the intact specimens, the specimens were deformed uniformly on the specimen surface before obvious cracks appeared on the surface. The accelerated deformation stage was relatively brief.

The strain distribution of the specimen was calculated based on the DIC method. Four stages were selected for strain cloud diagram representation: the stable deformation stage (a), the accelerated deformation stage (b), the crack propagation stage (c), and the specimen failure stage (d). The strain distribution of the specimen was shown in Fig.  $5\,b-h$ . Furthermore, based on the strain results obtained from the DIC method, the maximum equivalent strain, average equivalent strain of the specimens were calculated, and the results were presented in Table 2.



**Fig. 5.** Strain map of intact specimen and prefabricated fissure specimen: a – schematic diagram of the deformation stage of the specimen; b – intact specimen; c – specimen with 0° fissure; d – specimen with 30° fissure; e – specimen with 45° fissure; f – specimen with 60° fissure; g – specimen with 75° fissure; h – specimen with 90° fissure

Table 2. Statistical table of surface strain of specimens

Type	Maximum equivalent strain			Average equivalent strain				
	1	2	3	4	1	2	3	4
Intact	0.0374	0.0435	0.0499	0.2239	0.0023	0.0032	0.004	0.0066
0°	0.0377	0.0459	0.0567	0.2214	0.0017	0.0027	0.0045	0.0075
30°	0.0249	0.0286	0.060	0.13937	0.002	0.0043	0.0066	0.0091
45°	0.0241	0.046	0.0662	0.1108	0.0021	0.0034	0.0068	0.0089
60°	0.0188	0.026	0.058	0.1543	0.0015	0.0035	0.0058	0.0073
75°	0.0177	0.0268	0.0526	0.0776	0.0011	0.0019	0.004	0.0052
90°	0.0166	0.0298	0.0544	0.0834	9.3E-4	0.0016	0.0031	0.0047

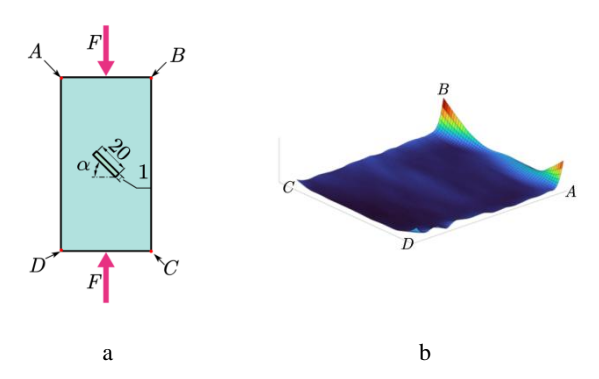


Fig. 6. Correspondence between specimen model and strain distribution location

### 4. ANALYSIS AND DISCUSSION

To examine the impact of the fissure inclination on the deformation and strain distribution of the specimen, we processed the data obtained by the DIC method. Based on the strain distribution matrix calculated by the DIC method,

a contour map of the specimen's strain distribution was plotted (as shown in Fig. 6, Fig. 7 and Fig. 8). Additionally, the changes in the maximum equivalent strain (Fig. 9) and the average equivalent strain (Fig. 10) of the specimen were quantified.

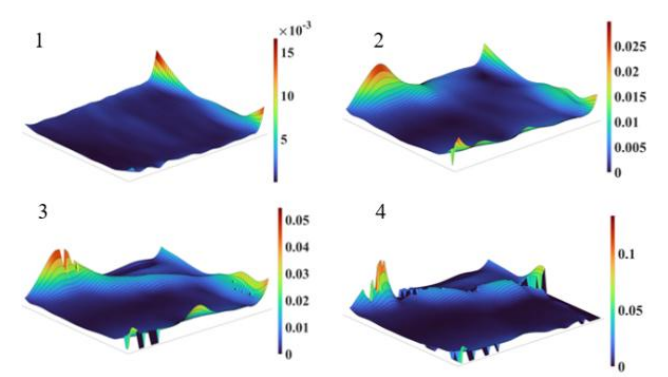
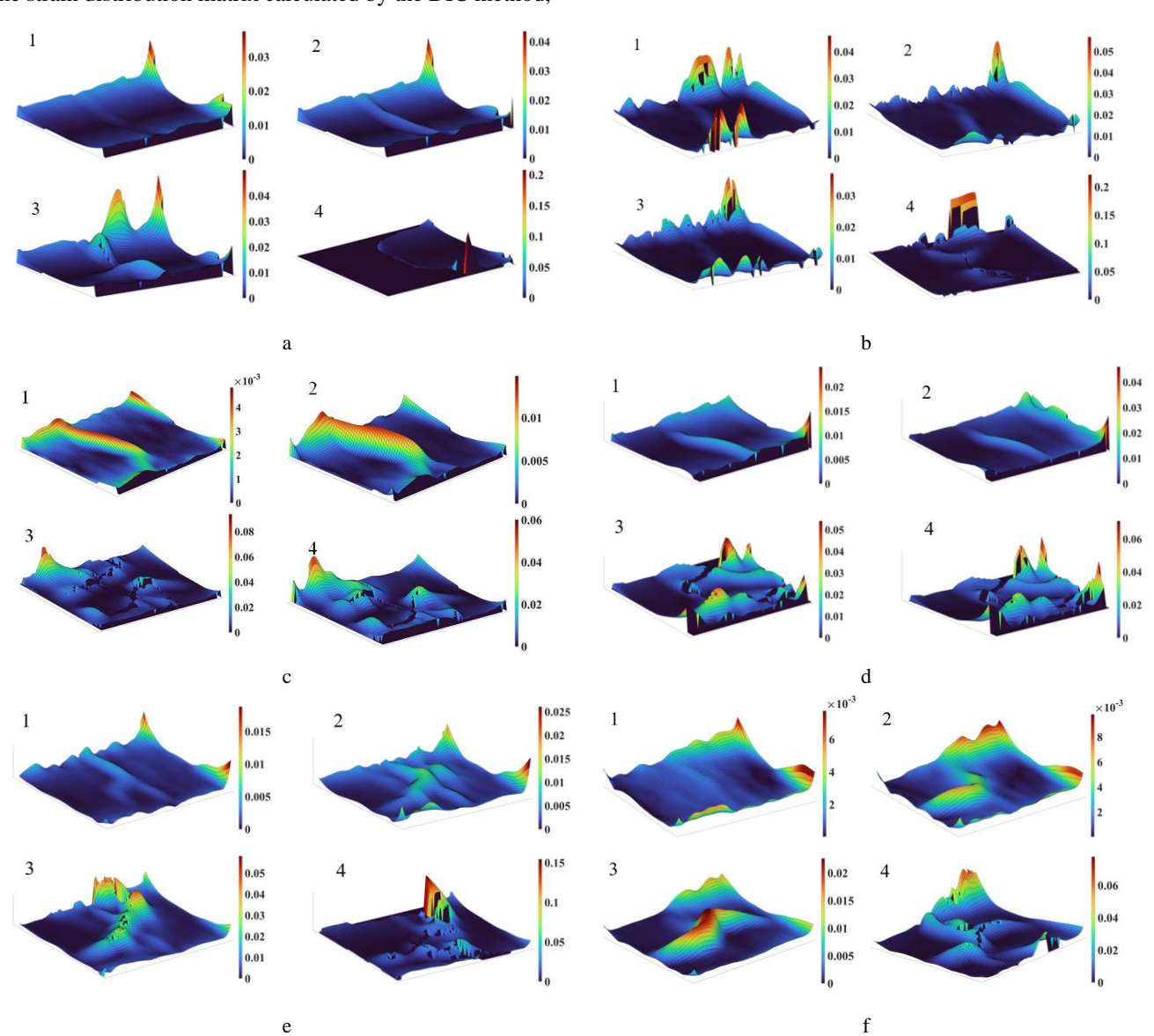


Fig. 7. Strain distribution of intact specimen



**Fig. 8.** Strain distribution of prefabricated fissure specimen: a – fissure inclination 0°; b – fissure inclination 30°; c – fissure inclination 45°; d – fissure inclination 60°; e – fissure inclination 75°; f – fissure inclination 90°

# 4.1. Analysis of influence of fissure inclination on strain distribution

As illustrated in Fig. 5 and Fig. 7, the strain distribution diagram and strain contour diagram, respectively, indicated that for the intact specimen in the stable deformation stage, the majority of the strain was concentrated in the upper portion of the specimen, with a maximum strain value of approximately 0.016. This was attributable to the fact that, at the lower load level, the overall specimen deformation was relatively minor, resulting in a comparatively significant strain at the upper portion of the specimen where stress was concentrated. As the load increased, the specimen exhibited a gradual deformation, with the maximum strain transferred to the lower right end of the specimen. For the sandstone-like specimen, damage was mainly dominated by shear-slip damage. Consequently, the intact sandstone-like specimen produced a large strain in the lower right corner of the specimen at a certain angle with the principal stress. The maximum strain of the specimen was 0.054.

The specimen began to produce visible cracks as the load continues to increase, and entered the crack propagation stage. Cracks propagated rapidly and were at an angle to the principal stress. With the continued expansion of cracks, the cracks increased significantly, resulting in specimen damage. The damage to intact specimen exhibited characteristics of shear-slip pattern, with the maximum strain of the specimen reaching 0.083. As illustrated in Fig. 7, the deformation of the specimen to the intact specimen was relatively minor, with a significant local deformation occurring only in the lower right corner of the crack. The distribution of strains observed in the fissured specimens exhibited a divergence from that observed in the intact specimen. Fig. 8 a-f revealed that during the stable deformation stage, the maximum strain of the fissured specimen occurred at the point of contact between the loading device and the upper end face of the specimen. However, in contrast to the intact specimen, the fissured specimens exhibited considerable strain near the fissure. The maximum strain reached 0.0177-0.0377 during the stable deformation stage, representing a 6.63 % to 127.11 % increase compared to the intact specimen. This phenomenon might be attributed to the fact that the stress concentration at the fissure tips was readily produced, resulting in increased deformation in the stress concentration area. Oin<sup>[24]</sup> also observed in his experiments that there was a significant stress concentration phenomenon at the tip of the fissure, leading to the emergence of new cracks in the tip area first.

The maximum equivalent strain of the specimens' inclination from  $0^{\circ}$  to  $60^{\circ}$  at the stable deformation stage increased by 45.18 % to 127.11 % compared to the intact specimens. The variation in the maximum equivalent strain at fissure inclinations between 75° and 90° is minimal, exhibiting a discrepancy of only 6.63 % to 13.25 % compared to the intact specimen. This indicated that the presence of fissure increased the deformation of the specimen within the stable deformation stage, and the increase was related to the fissure inclination. The closer the inclination was to the principal stress direction (i.e. the closer it is to  $90^{\circ}$ ), the closer the maximum equivalent strain at the stable deformation stage of the specimen was to that

of the intact specimen. Conversely, as the fissure inclination aligned closer to the direction perpendicular to the principal stress direction (i.e. the direction of  $0^{\circ}$ ), a more significant increase in maximum equivalent strain at the stable deformation stage was observed.

As the load increased, the specimen reached the accelerated deformation stage, accompanied by an increase in the strains on the left and right sides. From the strain contour map, it can be observed that the strain in the fissure region exhibited non-uniform distribution characteristics, with the maximum equivalent strain occurring in the area in close proximity to the fissure. The strain discrepancy between the fissured and intact specimens decreased in accelerated deformation stage. For example, the strain of fissure specimens with inclinations of 45°, 75° and 90°in accelerated deformation stage were reduced by only 4.03 %, 12.75 % and 10.07 % compared to the intact specimen, and the magnitude of strain change was further reduced. This may be due to the fact that the significant deformation in stable deformation stage had resulted in the closure of fissure, thereby resulting in the strain of the fissured specimen more closely aligned with that of the intact specimen in accelerated deformation stage.

The majority of these cracks occurred in close proximity to the fissure tips. The difference in strain between the fissured and the intact specimen were further diminished, with the gap in strain not exceeding 10.29 %. This indicated that the strain gap was insignificant when the specimen was in the initial phase of cracking. The strain of the fissured specimens exhibited an increase in comparison to the intact specimens when the specimens were damaged. The maximum increase reached 168.47 %, which was observed when the inclination angle of the fissure was 0°. This indicated that the presence of the fissure resulted in a notable intensification of deformation during the failure stage.

# **4.2.** Analysis of the influence of fissure inclination on strain parameters

In order to reveal the influence of fissure inclination on the strain parameters, a count was made of the maximum and average equivalent strain at four stages. Fig. 9 and Fig. 10 revealed that the maximum and average equivalent strain of the specimens increased gradually with increasing load. Based on the strain distribution, we analyzed the effect of fissure inclination on the strain evolution. Fig. 9 illustrated that the maximum equivalent strain of the intact specimen and the specimen with a 90° fissure inclination increased in a uniform manner with increasing loads. The maximum equivalent strain was approximated by a straight line. The maximum equivalent strain of fissured inclination among 0° and 75° exhibited a gradual increase before the appearance of cracks. Following the generation of cracks, the equivalent train increased markedly, which may be attributed to the elevated strain resulting from the closure of the prefabricated fissures before the emergence of cracks. Once cracks are generated, the equivalent strain increased significantly with the expansion of these cracks. For instance, in fissure specimens with an inclination of 0° and 30°, the equivalent strain at the accelerated deformation stage were 0.044 and 0.046, respectively.

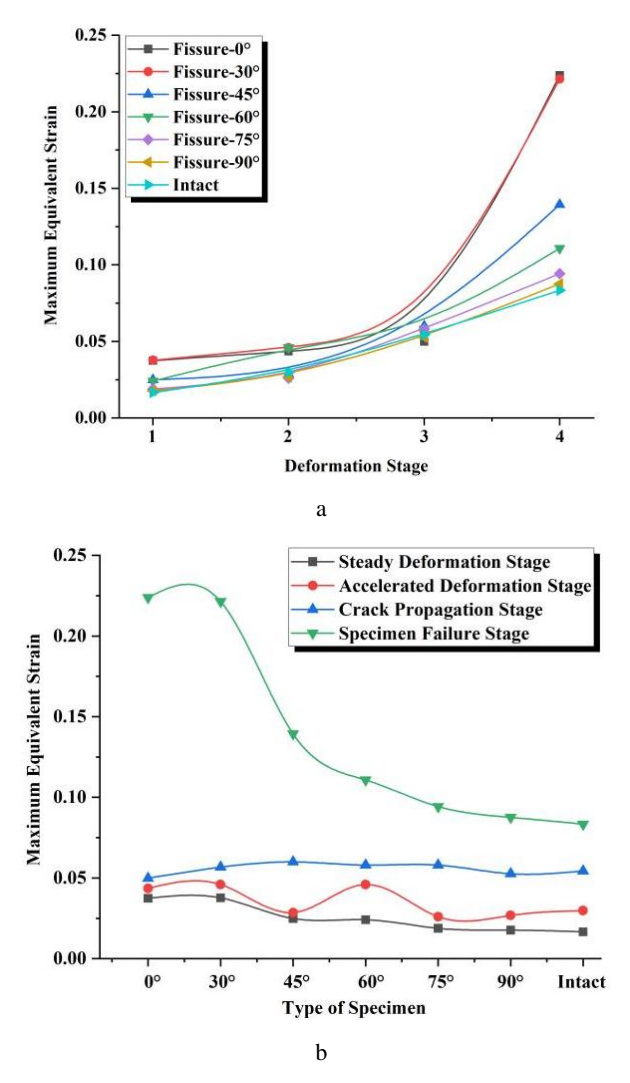


**Fig. 9.** Trend of maximum equivalent strain of specimen: a – variation trend in strain at different stages; b – variation trend of strain with fissure inclination

While the equivalent strain were 0.224 and 0.221 at specimen failure stage, the increase was 409.1 % and 380.4%, respectively. In contrast, for intact specimens, the increase in specimen failure stage was only 182.9 %. Fig. 9 b revealed that the maximum equivalent strain in the stable deformation stage declined as the inclination increased. Furthermore, the maximum equivalent strain of the intact specimen was the lowest. In the accelerated deformation and crack propagation stages, the maximum equivalent strain exhibited an initial increase, followed by a subsequent decrease with the increase of the fissure inclination. The equivalent strain of the specimen reached the maximum value in proximity to the inclination of 60°. Nevertheless, the variation of the maximum equivalent strain of the specimen was minimal, amounting to only 54.36 % and 10.29 %, respectively. Accordingly, it can be inferred that the influence of the fissure inclination on the deformation of the specimen was insignificant in these two stages. The deformation was largest at the inclination of 0°, with a subsequent gradual decreased in deformation as the inclination increased.

In conclusion, the strain changed in the stable deformation stage and specimen failure stage are the most significant, with increases of 127.11 % and 168.47 %,

respectively. This suggested that the impact of fissure inclination on the deformation of the damaged rock mass was predominantly evident during the stable deformation and specimen failure stages. Prior to the closure of the prefabricated fissure and following the emergence of new cracks, the prefabricated fissure exerted a considerable influence on the deformation and destruction of the specimen.

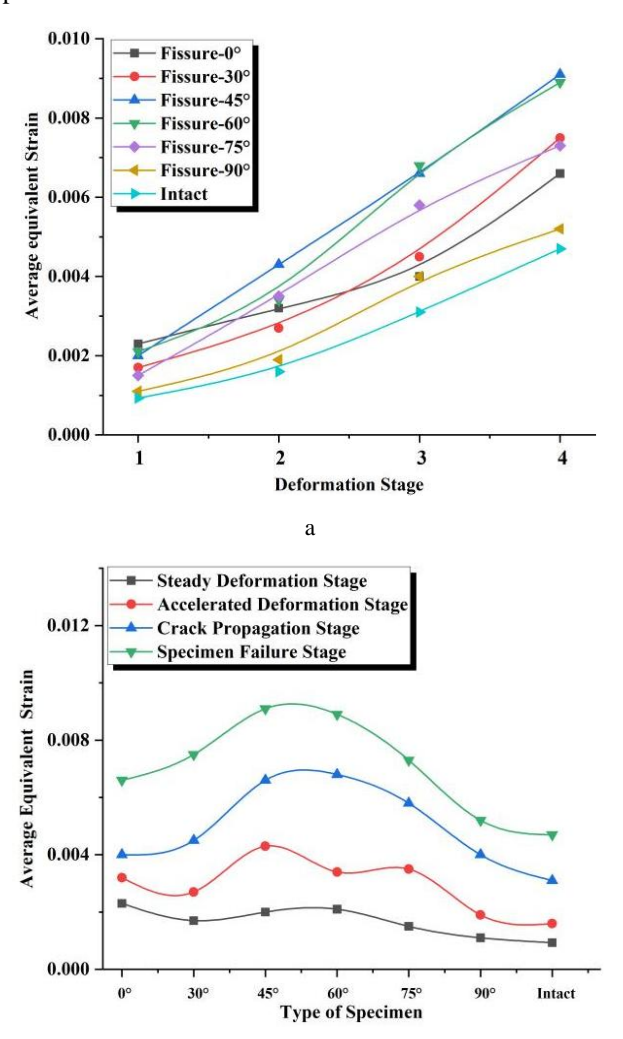


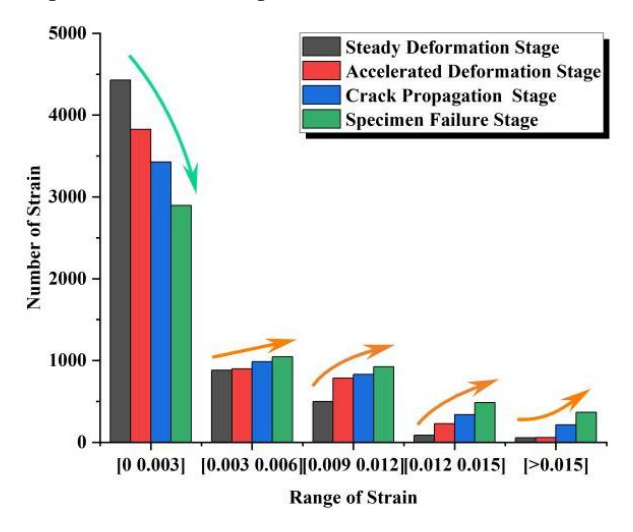
**Fig. 10.** Trend of average equivalent strain of specimen: a – variation trend in strain at different stages; b – variation trend of strain with fissure inclination

b

The trend of the average equivalent strain with the fissure inclination was calculated and analyzed (see Fig. 10). The results are shown in Fig. 10 a), which indicated that the average equivalent strain on both intact specimens and fissured specimens increased with the load. However, the trend and the difference between the average equivalent strains of the two type specimens were smaller in comparison to the maximum equivalent strain. It is due to the undamaged area accounts for a large proportion in fissured specimen.

A comparison of the strain sizes of the intact specimen and the fissured specimen (with a 0° fissure as an example) (Fig. 11) revealed that the strains of the two types specimens were dominated by the small-sized strains of less than 0.003. The fissured specimens exhibited a greater proportion of

large-size strains (> 0.015) in the accelerated deformation stage, crack propagation stage, and specimen failure stage compared to the intact specimens.



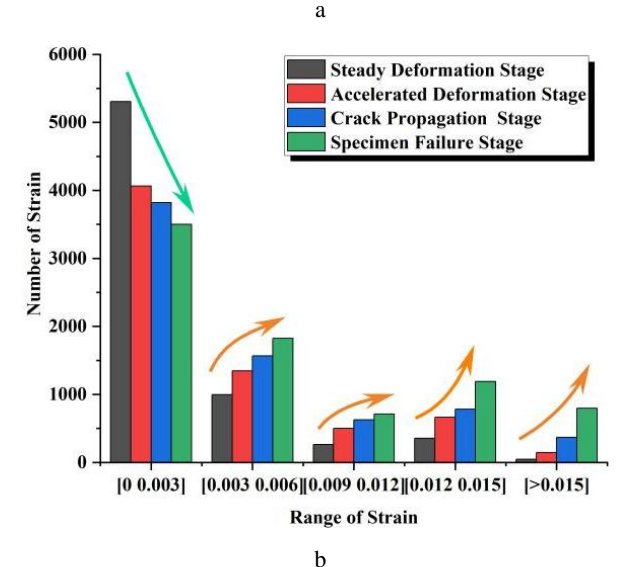


Fig. 11. Strain size statistics for intact and fissure specimens: a-intact specimen; b-fissure specimen (fissure inclination  $0^{\circ}$ )

The proportion of strains exceeding 0.015 in the overall strain was relatively minor. As illustrated in Fig. 11, the proportion of strains exceeding 0.015 in the intact specimen ranges from 1.0 % to 6.4 %. The proportion of strains greater than 0.015 in the fissured specimen ranges from 2.1 % to 9.9 %. Consequently, there was not a significant difference between the fissured and intact specimens on average regarding to average equivalent strains.

In comparison to the intact specimen, the average equivalent strain of the fissure specimen was consistently higher at all stages. This was primarily attributable to the fissure will be closed, allowing for greater deformation than that observed in the intact specimen.

The average equivalent strain on the surface of the specimens with different prefabricated fissure inclinations was also different. As illustrated in Fig. 10 b, the closer the fissure inclination angle was to 45°, the larger the mean equivalent strain of the specimen. Conversely, the closer the fissure inclination angle was to 90°, the closer the mean

equivalent strain of the specimen was to that of the intact specimen. In the stable deformation stage, the average equivalent strain of the specimen was relatively insensitive to the fissure inclination angle. As the fissure inclination angle increased, the average equivalent strain of the specimen decreased. In the accelerated deformation stage, crack propagation stage, and specimen failure stage, the average equivalent strain of the specimen exhibited a general increase followed by a subsequent decrease with the increase of the fissure inclination angle. The maximum value was observed within the range of fissure inclination angles between 45° and 60°. In comparison to the intact specimen, the maximum values of the average equivalent strain in the four stages exhibited a notable increase, reaching 147.31 %, 168.75 %, 119.35 %, and 93.62 %, respectively.

The results demonstrated that the deformation of the specimen was significantly influenced by the fissure inclination angle. The analysis indicated that the angle between 45° and 60° had the greatest influence on the specimen's deformation. This trend coincided with the nominal strain calculated through the measurement of deformation using the material mechanics testing machine [25, 26].

It has been demonstrated through comprehensive analysis that the existence of fissures had a discernable impact on the deformation of the specimen. The magnitude of this effect was related to the angle between the fissure and the principal stress direction. It had been established that as the inclination angle of the fissure approached 45°, the influence of the fissure on the deformation of the specimen increased. Conversely, as the inclination angle of the fissure approached 90°, the influence of the fissure on the deformation of the specimen decreased. The maximum equivalent strain of the specimen was related to the stress distribution in the near area of the fissure. The strain in the area of stress concentration was relatively large. Furthermore, the closer the fissure of the specimen was to 0°, the larger the deformation of the specimen was when it was damaged.

#### 5. CONCLUSIONS

In this paper, prefabricated fissures were introduced into sandstone-like specimens to simulate the internal damage of rock masses for mechanical testing. The digital image correlation method was employed to analyze the evolution of specimen surface strain parameters and crack extension patterns, and to investigate the influence of fissure inclination on the deformation of damaged rock masses. The findings revealed that:

- The digital image correlation method revealed that both intact specimens and prefabricated fissure specimens exhibited a stable deformation stage, an accelerated deformation stage, a crack propagation stage and a specimen failure stage. However, the accelerated deformation stage of the fissure specimen was longer in duration and the nascent cracks on the specimen surface were more pronounced.
- It is possible that stress concentration occurred at the fissure tip, and new cracks formed at the fissure tip and then expanded in the direction of principal stresses. The

- maximum equivalent strain of the specimen in the range of fissure inclination angle  $0 \sim 75^{\circ}$  showed a pronounced increase. At the fissure inclination angle of  $90^{\circ}$ , there is no change in the trend of strain change before and after the appearance of crack in the specimen.
- 3. The prefabricated fissure affected the deformation of the specimen. The greater the perpendicularity of the crack to the principal stress direction, the greater the deformation of the specimen. Conversely, the greater the parallelism of the fissure to the principal stress direction, the smaller the deformation of the specimen. The inclination angle of the prefabricated fissure exerts the greatest influence on the deformation of the specimen within the range of 45° to 60°.

### Acknowledgments

This research was funded by the Scientific Research Foundation of Weifang University grant number [2021BS24] and the APC was funded by Weifang University. The authors wish to acknowledge these supports. At the same time, authors are very grateful for the anonymous reviewers' valuable comments.

#### REFERENCES

- 1. **Yang, G., Xie, D., Zhang, C.** CT Identification of Rock Damage Properties *Chinese Journal of Rock Mechanics and Engineering* 1996 (01) 1996: pp. 48–54.
- Yang, G., Xie, D., Zhang, C. CT Analysis on Mechanical Characteristics of Damage Propagation of Rock *Chinese* Journal of Rock Mechanics and Engineering 1999 (03) 1999: pp. 250–254.
- Zhang, C., Jia, S., Ren, Z.P. Strength Evolution Characteristics of Coal with Different Pore Structures and Mineral Inclusions Based on CT Scanning Reconstruction Natural Resources Research 2024 (33) 2024: pp. 2725 – 2742. https://doi.org/10.1007/s11053-024-10397-3
- Wang, X.R., Shan, T.C., Liu, S.X., Thermal-Damage Effects on Fracturing Evolution of Granite under Compression-Shear Loading Theoretical and Applied Fracture Mechanics 2024 (133) 2024: pp. 104581. https://doi.org/10.1016/j.tafmec.2024.104581
- Zhao, F., Shi, Z.M., Yu, S.B. A Review of Fracture Mechanic Behaviors of Rocks Containing Various Defects Underground Space 2023 (12) 2023: pp. 102 – 115. https://doi.org/10.1016/j.undsp.2023.02.006
- 6. **Li, Y.P., Chen, L.Z., Wang, Y.H.** Experimental Research on Pre-cracked Marble under Compression *International Journal of Solids and Structures* 42 (9) 2005: pp. 2505–2516. https://doi.org/10.1016/j.ijsolstr.2004.09.033
- Wang, C., Li, Y., Dai, F. Experimental Investigation on Mechanical Properties and Failure Mechanism of Rock-Like Specimens Containing an Arc-Shaped Ice-Filled Flaw under Uniaxial Compression Theoretical and Applied Fracture Mechanics 2022 (119) 2022: pp. 103368. https://doi.org/10.1016/j.tafmec.2022.103368
- Li, X.W., Yao, Z.S., Huang, X.W. Mechanical Properties and Energy Evolution of Fractured Sandstone under Cyclic Loading *Materials* 15 (17) 2022: pp. 6116. https://doi.org/10.3390/ma15176116

- 9. **Liu, L.W., Li, H.B., Li, X.F.** Underlying Mechanisms of Crack Initiation for Granitic Rocks Containing a Single Preexisting Flaw: Insights From Digital Image Correlation (DIC) Analysis *Rock Mechanics and Rock Engineering* 54 (2) 2021: pp. 857 873. https://doi.org/10.1007/s00603-020-02286-x
- Tian, S., Zhao, Y., Hu, S. Experimental Study on Freeze-Thaw Damage Characteristics and Mechanical Properties of Fractured Rock Mass of Open-Pit Mine Slope in Cold Region *Journal of China Coal Society* 2024: pp. 1–16. https://doi.org/10.13225/j.cnki.jccs.2024.0474
- 11. **Tang, S.C., Peng, F., Zhao, J.C.** Uniaxial Mechanical Properties and Failure Mechanism of Rock Specimens Containing Cross Fissures *Chinese Journal of Underground Space and Engineering* 17 (05) 2021: pp. 1376–1383+1407.
- 12. **Song, Y.J., Cheng, K.Y., Meng, F.D.** Research on Acoustic Emission Characteristics of Fractured Rock Damage under Freeze-Thaw Action *Journal of Mining & Safety Engineering* 40 (02) 2023: pp. 408–419. https://link.oversea.cnki.net/doi/10.13545/j.cnki.jmse.2022.0 139
- Quan, D.G., Lian, S.L., Bi, J. Analysis of Mechanical Properties of Sandstone under Freeze-Thaw Cycles Based on Digital Image Correlation (DIC) Geofluids 2021 2021: pp. 1–12. https://doi.org/10.1155/2021/7101873
- 14. Luo, F., Gao, S., Xu, Z.M., Dong, E.Y., Diao, Y.M., Sang, Y.T. Mechanical Behavior and Tension-Shear Failure Mechanism of Fractured Rock Mass under Uniaxial Condition *Bulletin of Engineering Geology and the Environment* 82 (314) 2023: pp. 314. https://doi.org/10.1007/s10064-023-03330-0
- 15. Cao, Y., Chen, L., Xu, J.H. Unified Analytical Solutions of Circular Tunnel Excavated in an Elastic-Brittle-Plastic Rock Mass considering Blast-Induced Damage and Dead Weight Loading Advances in Civil Engineering 2021 2021: pp. 1 – 12. https://doi.org/10.1155/2021/5537963
- Li, Y.G., Zhang, H.M., Chen, M. Strength Criterion of Rock Mass Considering The Damage and Effect of Joint Dip Angle Scientific Reports 12 (1) 2022: pp. 2601. https://doi.org/10.1038/s41598-022-06317-1
- 17. Zhao, Y.H., Liang, H.H., Xiong, C.Y. Deformation Measurement of Rock Damage By Digital Image Correlation Method Chinese Journal of Rock Mechanics and Engineering 2002 (01) 2002: pp. 73-76.
- Li, B.L., Sun, T., Zhang, J.Z. Mechanical and Failure Characteristics of Flawed Granite after High-Temperature Cycling: An Experimental Study using Biaxial Compression Theoretical and Applied Fracture Mechanics 2024 (133) 2024: pp. 104601. https://doi.org/10.1016/j.tafmec.2024.104601
- Zhou, T., Chen, J.R., Xie, H.P. Failure and Mechanical Behaviors of Sandstone Containing a Pre-existing Flaw Under Compressive–shear Loads: Insight from a Digital Image Correlation (DIC) Analysis *Rock Mechanics and Rock Engineering* 55 (7) 2022: pp. 4237 – 4256. https://doi.org/10.1007/s00603-022-02861-4
- Zhu, X., Fan, J., He, C.L. Identification of Crack Initiation And Damage Thresholds in Sandstone using 3D Digital Image Correlation Theoretical and Applied Fracture Mechanics 122 2022: pp. 103653. https://doi.org/10.1016/j.tafmec.2022.103653

- Wang, P.T., Liu, Q.R., Zhang, Y.S. Identifying Rock Fracture Precursor by Multivariate Analysis Based on The Digital Image Correlation Technique *Theoretical and Applied Fracture Mechanics* 126 2023: pp. 103987. https://doi.org/10.1016/j.tafmec.2023.103987
- 22. Maruschak, P.O., Konovalenko, I.V., Bishchak, R.T. Effect of Thermal Fatigue Cracks on Brittle-Ductile Deformation and Failure of Cbcm Roller Surface Layers Metallurgist 56 2012: pp. 30–36. https://doi.org/10.1007/s11015-012-9532-9
- 23. **Wang, Y.Y., Wang, H.W., Shi, X.** Creep Investigation on Shale-Like Material with Preexisting Fissure under Coupling Temperatures and Confining Pressures *Advances in Civil Engineering* 2019 2019: pp. 1–10. https://doi.org/10.1155/2019/7861305
- 24. Qin, Y., Xu, N.X., Han, J. Experimental Study on the Effects of Geometric Parameters of Filled Fractures on the

- Mechanical Properties and Crack Propagation Mechanisms of Rock Masses *Rock Mechanics and Rock Engineering* 56 (4) 2023: pp. 2697 2716. https://doi.org/10.1007/s00603-022-03198-8
- Zhang, X., Li, X.S., Liu, Y.H. Experimental Study on Crack Propagation and Failure Mode of Fissured Shale under Uniaxial Compression Theoretical and Applied Fracture Mechanics 121 2022: pp. 103512. https://doi.org/10.1016/j.tafmec.2022.103512
- 26. Zheng, M.H., Liang, Y.P., Staat, M. Discontinuous Fracture Behaviors and Constitutive Model of Sandstone Specimens Containing Non-Parallel Prefabricated Fissures under Uniaxial Compression *Theoretical and Applied Fracture Mechanics* 131 2024: pp. 104373. https://doi.org/10.1016/j.tafmec.2024.104373



© Wang et al. 2025 Open Access This article is distributed under the terms of the Creative Commons Attribution 4.0 International License (http://creativecommons.org/licenses/by/4.0/), which permits unrestricted use, distribution, and reproduction in any medium, provided you give appropriate credit to the original author(s) and the source, provide a link to the Creative Commons license, and indicate if changes were made.